Cortical seizure propagation respects functional connectivity underlying sensory processing

L Federico Rossi[1], Robert C Wykes[2], Dimitri M Kullmann[2], Matteo Carandini[1]

[1]UCL Institute of Ophthalmology and [2]UCL Institute of Neurology, University College London

Focal epilepsy involves excessive and synchronous cortical activity that propagates both locally and distally. Does this propagation follow the same routes as normal cortical activity? We induced focal seizures in primary visual cortex (V1) of awake mice, and compared their propagation to the retinotopic organization of V1 and higher visual areas. We measured activity through simultaneous local field potential recordings and widefield imaging of a genetically encoded calcium indicator, and observed both prolonged seizures (ictal events) and brief interictal events. Both types of event were orders of magnitude larger than normal visual responses, and both started as standing waves: synchronous elevated activity in the focal V1 region and in corresponding retinotopic locations in higher areas. Following this common beginning, however, seizures, persisted and propagated both locally and into distal regions. These regions matched each other in retinotopy. We conclude that seizure propagation respects the functional connectivity underlying normal visual processing.

Focal epilepsy, also known as partial-onset epilepsy, can result from a range of congenital or acquired cortical lesions and frequently resists pharmacological treatment[1]. Much of its morbidity results from the spread of seizure activity from a cortical focus to further cortical regions. These regions can be local and contiguous to the focus, as in the "Jacksonian march" seen in motor cortex. However, they can also be distal and ultimately involve both hemispheres and subcortical centers ("secondary generalization"), causing loss of consciousness[2].

It is not known whether seizures spread along the same functional circuits that support information processing during normal cortical activity[3]. These circuits may not act as effective constraints during seizures. First, functional circuits rely on synaptic transmission, whereas seizures may involve non-synaptic mechanisms[4–11]. Second, the flow of activity along functional circuits depends on the balance of synaptic excitation and inhibition, and seizures disrupt this balance[12–16].

A related question concerns the difference between seizures (ictal events), and the numerous, brief interictal discharges that characteristically occur between seizures. Seizures represent excessive neuronal firing lasting seconds or minutes and spreading locally and distally[12,17]. Interictal discharges, instead, are brief and localized[18]. A longstanding theory is that their duration and spread are limited by a powerful inhibitory surround[19]. It is not known, however, if seizures and interictal events originate in similar neuronal populations, and if their initiation differs in terms of spatial profile and temporal evolution[20]. More generally, it is not clear why seizures persist and propagate, while interictal discharges subside and stay local.

We addressed these questions in the visual cortex of the mouse, where we could readily distinguish between two scenarios of seizure propagation (Figure 1**a**-**d**). Mouse visual cortex includes multiple retinotopic areas[21–23], the largest of which are the primary and latero-medial areas (V1 and LM, Figure 1**a**). Epileptiform activity in a focal region of V1 (Figure 1**b**) could then spread in at least two ways: laterally or homotopically. In the first scenario, epileptiform activity propagates through local mechanisms to V1 regions that are contiguous to the focus (Figure 1**c**). In the second scenario, epileptiform activity propagates along long-range projections from V1 to homotopic regions of higher visual areas, i.e. regions that have the same retinotopic preference[23,24] producing one or more distinct, secondary foci (Figure 1**d**).

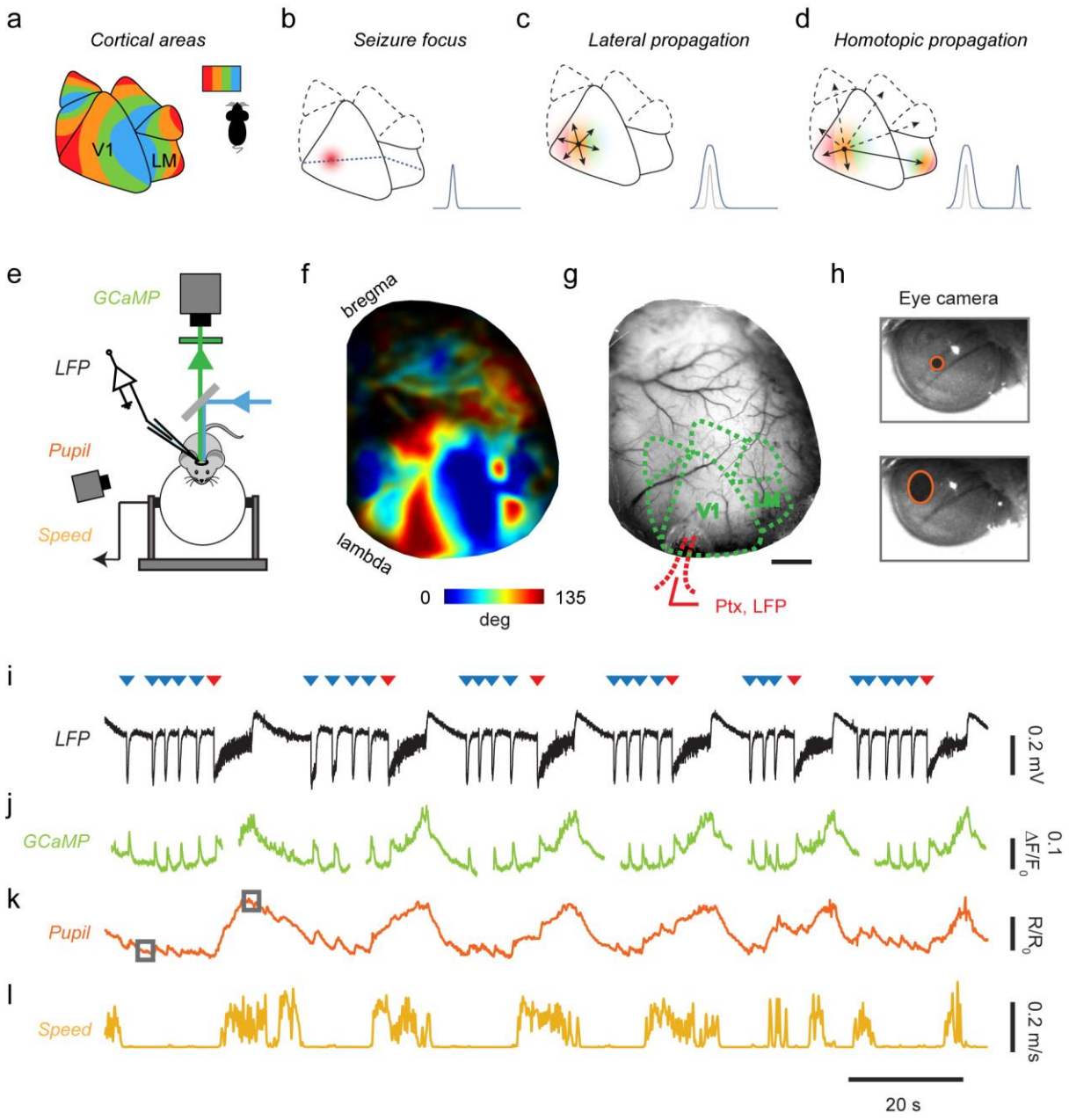

Figure 1: Simultaneous widefield GCaMP imaging, LFP recordings and behavioral measurements to study seizure propagation in the visual cortex. (**a**) Cartoon of mouse visual cortex showing 6 visual areas in the right hemisphere, each containing a map of the left visual field (*inset*). Colors indicate territories that prefer the same horizontal position. Labels indicate the primary and secondary visual area (V1 and LM). (**b**) Cartoon depicting elevated activity in the seizure focus in V1. *Dotted line* through the epileptic focus connects V1 and LM regions that prefer the same vertical position. *Inset*: Profile of activity along that line. (**c**) Lateral propagation hypothesis: local mechanisms make seizure spread radially to nearby territories. *Inset*: profile of idealized activity at onset (*gray*) and during spread (*blue*). (**d**) Homotopic propagation hypothesis: long-range connections generate secondary distal foci in homotopic locations in higher visual areas. *Inset* as in **c**. (**e**) Schematic of the experimental setup. (**f**) Example retinotopic map obtained from a GCaMP6f mouse. Colors indicate preferred horizontal position. (**g**) Representative image acquired during simultaneous widefield imaging and LFP recordings. *Red dots* highlight location in V1 of pipette for injection of Picrotoxin (Ptx) and recordings of local field potential (LFP). *Scale bar* indicates 1 mm**.** (**h**) Example frames from the eye camera taken when the pupil was constricted (*top*) or dilated (*bottom*), with fitted ellipses (*red*). (**i**) LFP traces measured during epileptiform activity showing seizures (*red triangles*) and interictal discharges (*red triangles*). (**j**) Simultaneous GCaMP fluorescence, averaged over the entire imaging window (discontinuities indicate pauses in image acquisition). (**k**-**l**) Behavioral correlates of the epileptiform discharges: pupil dilations (**k**) and running speed (**l**).

To evaluate these models of seizure propagation, we induced epileptiform activity in a focal region of V1 and used widefield imaging of genetically-encoded calcium indicators[25,26] to characterize the propagation of activity in space and time. These methods allowed us to observe both prolonged seizures (ictal events) and brief interictal events, and to relate their spatiotemporal

evolution to the functional connectivity underlying normal visual processing.

Results

We generated transgenic mice expressing a genetically-encoded calcium indicator (GCaMP3 or GCaMP6) in excitatory neurons of the cortex[27–29], and implanted a head-post and a cranial window spanning the left parietal bone, which we thinned to facilitate optical access[26]. After recovery and a period of habituation, we head-fixed the mice over a treadmill where they were free to run while we performed visual stimulation, widefield imaging, and electrophysiological recordings (Figure 1**e**).

We first used widefield imaging of GCaMP fluorescence to measure activity evoked by visual stimulation, and mapped the retinotopic organization of V1 and higher visual areas (Figure 1**f**). For each mouse we aligned the salient features of the retinotopic map[26] on a reference map of the areal organization of the mouse visual cortex[30]. This procedure identified multiple visual areas (Figure 1**f**) including V1 and adjacent area LM, which is thought[31] to be homologous to primate area V2.

We then elicited focal epileptiform discharges by blocking $GABA_A$ receptors in a small region of V1 (Figure 1**g**). $GABA_A$ receptors were blocked by including picrotoxin (10 mM) in a pipette inserted into medial V1 via a small craniotomy. We applied no pressure, so that the picrotoxin solution would diffuse minimally beyond the tip of the pipette (resistance 0.5-3 MΩ). We targeted layer 5 because its extensive recurrent, horizontal and columnar connectivity enable it to evoke prolonged depolarization across layers[32], making it a promising location for triggering translaminar epileptiform events.

Within minutes of pipette insertion, recordings of local field potential (LFP) made from the same pipette revealed robust epileptiform events (Figure 1**i-n**). These events consisted of intermittent seizures (Figure 1**i**, *red triangles*) separated by sequences of brief discharges (Figure 1**i**, *blue triangles*). These epileptiform events were mirrored by large amplitude GCaMP optical signals (Figure 1**l**). They were also typically accompanied by pronounced increases in pupil dilation (Figure 1**h**,**m**) and by bouts of running (Figure 1**n**).

Based on their duration, these epileptiform discharges could be readily categorized into distinct classes (Figure 2). The distribution of epileptiform discharge duration was bimodal (Figure 2**a**, $p < 0.001$, Wilcoxon rank sum test, n=5 mice), with a median duration of 8.6 s for seizures, and 0.5 s for interictal events. Interictal events occurred on average 13.4 ± 3.7 times per minute (n = 5 recordings in 5 animals), much more frequently than seizures, which occurred about once per minute (1.0 ± 0.2 events/min). Interictal events were slightly larger on average (Figure 2**b**, $p < 0.001$, Wilcoxon rank sum test, n = 5 mice) and were followed by briefer periods of relative LFP quiescence than seizures (Figure 2**c**).

Seizures had pronounced behavioral correlates: they were typically accompanied by prolonged pupil dilations (Figure 2**e**, **Suppl. Figure 1a**), by larger eye movements (not shown), and by bouts of running (Figure 2**f**, **Suppl. Figure 1b,** Kolmogorov-Smirnov test, $p < 0.01$, n = 5 mice). For interictal events, pupil dilations were typically smaller (Figure 2**e**), running bouts briefer (Figure 2**f**) and not consistent across mice (**Suppl. Figure 1b**).

Interictal and ictal events also had distinct spectral features (Figure 2**h**,**i**, **Suppl. Figure 2**). The LFP waveform of interictal events was highly stereotypical: a sharp negative deflection lasting 50-100 ms (Figure 2**h**, **Suppl. Figure 2a**). Seizures had similar onset (Figure 2**i**, **Suppl. Figure 2b**) , but this onset was followed by a rapid escalation of high-frequency activity, with a large increase in power between 8 and 30 Hz (**Suppl. Figure 2b**,**e**). The increase in power near 10 Hz was consistent across events and animals (**Suppl. Figure 2i**).

These epileptiform events were faithfully tracked by large fluorescence signals, which dwarfed those seen during normal visual processing (Figure 2**g**). The peak fluorescence changes (ΔF/F) seen during epileptiform events were 125±22% for interictal events and 175±50% for seizures. These signals were much larger than those evoked by visual stimuli[26,33] (Figure 2**g**), which peaked at 4±1%. Yet, they bore close relation-

ship to the LFP (**Suppl. Figure 3b**), and faithfully followed the main frequency components of seizures (Figure 2**j-k**).

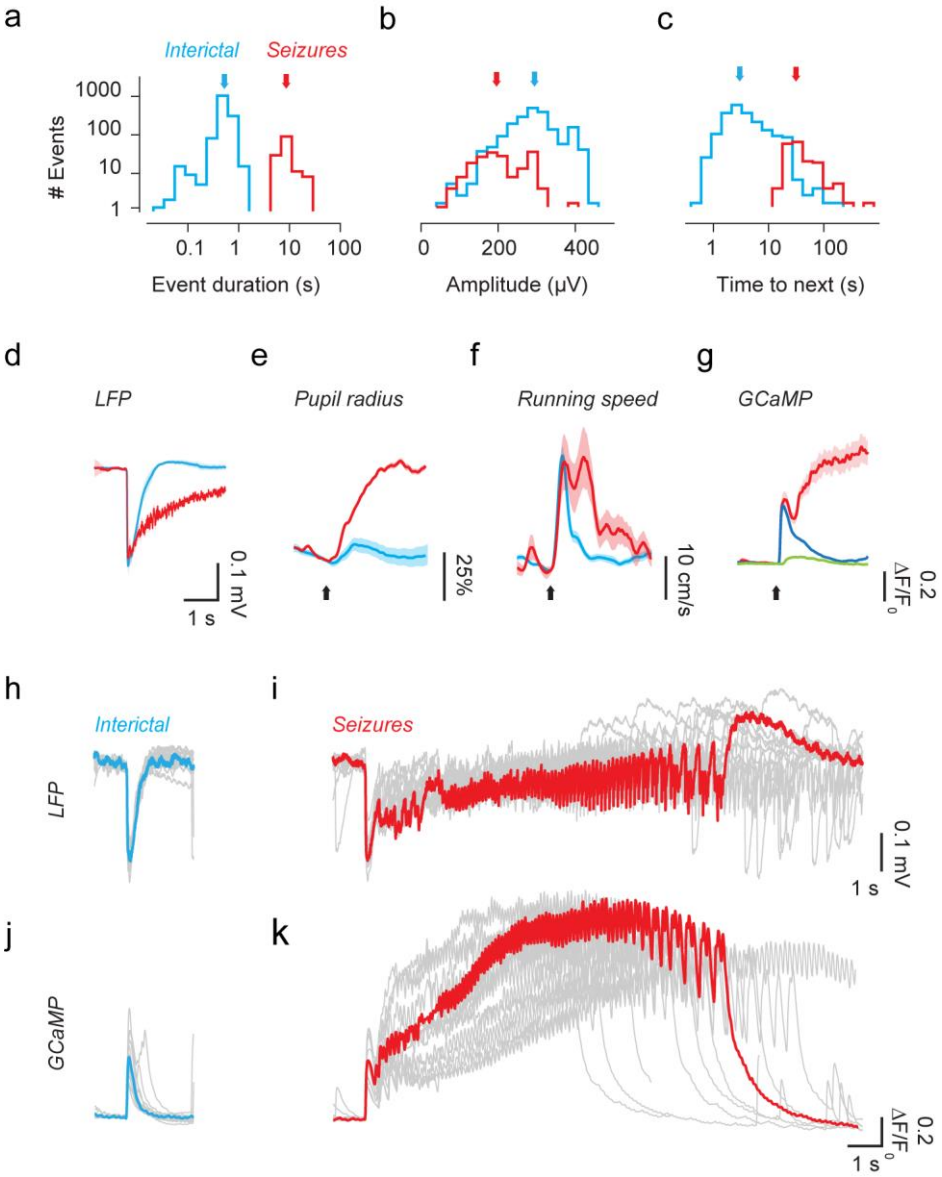

Figure 2: Neural and behavioral signatures of seizures and interictal discharges. (a) Distribution of the duration of interictal events (blue) and seizures (red). Arrows indicate the medians of each distribution. (b) Distribution of event amplitudes, measured as the peak of the initial LFP negative even. (c) Distribution of inter-event intervals (time to next event). (d) LFP waveform following the onset of interictal discharges (blue) and seizures (red), averaged across all events and animals (n = 5 mice). (e) Change in pupil radius triggered on the onset of interictal events (blue) and ictal events (red), for one representative animal. Arrow indicates discharge onset. (f) Same, for running speed. (g) Time courses of GCaMP activity in the same animal, averaged over area V1, during interictal events (blue) and seizures (red). Green trace shows response to flickering gratings for comparison. (h) LFP waveform of representative interictal events in one experiment. Blue trace highlights a single representative event. (i) Same as h, for seizures in the same experiment, with the representative trace in red. (j) GCaMP activity averaged over visual cortex during the example interictal events in h. (k) Same as j, for the seizures shown in i.

The fluorescence signals allowed us to study the spatial spread of epileptiform events, and revealed profound differences between ictal and interictal events (Figure 3**a-c**). The transient fluorescent signals seen during interictal events were localized in V1 with a smaller peak in LM (Figure 3**a**). They involved a region that was markedly smaller than the region that could be activated by visual stimuli (Figure 3**b**, Suppl. Movie 1). Seizures, instead, progressively invaded the entire visual cortex and beyond (Figure 3**c**, Suppl. Movie 2). Interictal and ictal events had similar origins: 94±4% of events started in V1, close to the pipette used to apply

picrotoxin and record LFP (starting positions were within a radius of 0.32±0.12 mm).

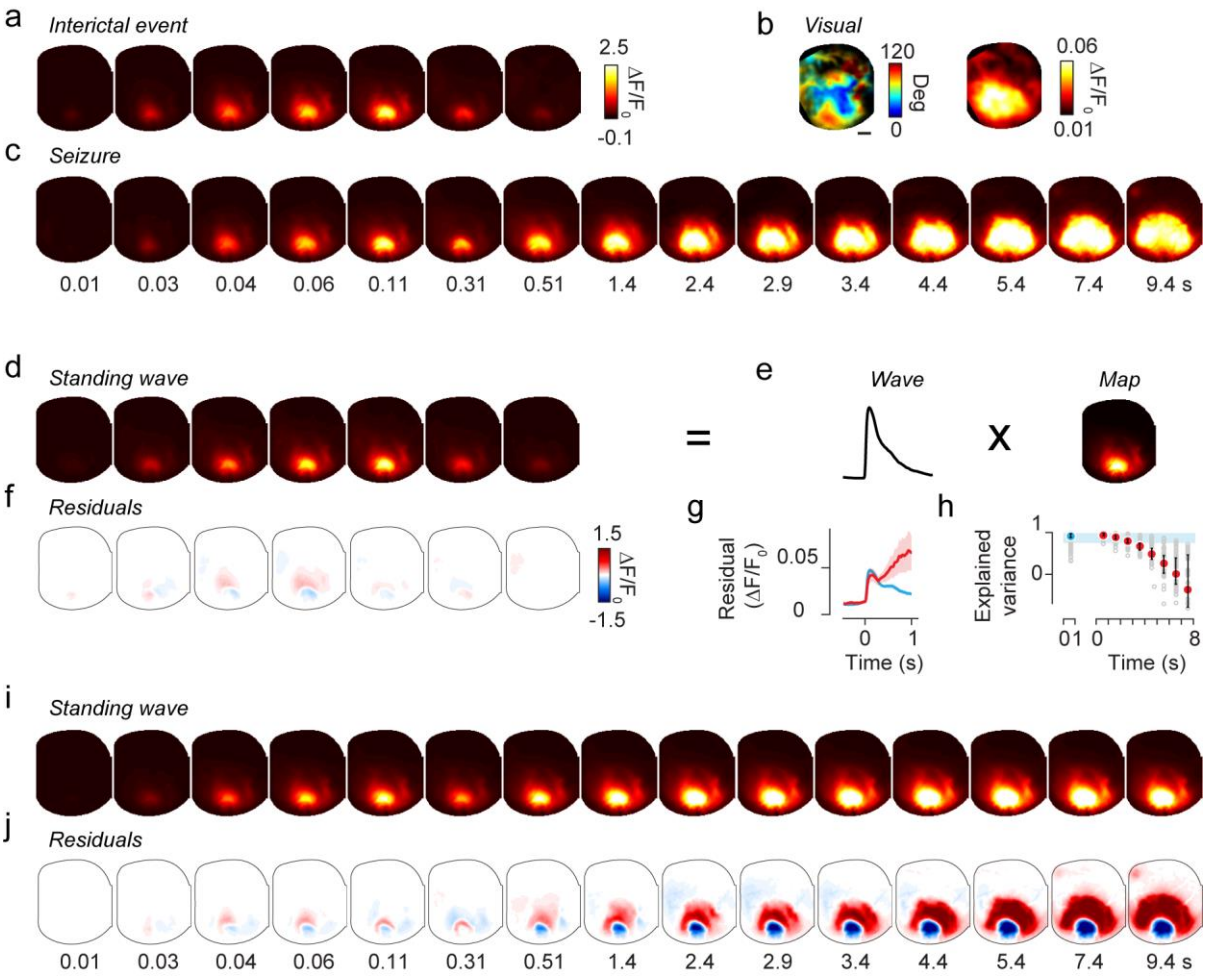

Figure 3: Interictal events and seizures start as standing waves, and seizures subsequently propagate widely across cortex. (**a**) Frames obtained through GCaMP imaging in a representative interictal event (the one highlighted in Figure 2**h**,**j**). (**b**) Retinotopic map and map of maximal activation in response to visual stimulation for the same animal as **a**. Scale bar is 1 mm. (**c**) Same as **a**, for a representative seizure (the one highlighted in Figure 2**i**, **k**). Time stamps indicate time of each frame from event onset and apply also to frames in **a**. (**d**) Predictions of a standing wave model fit to interictal event in **a**. (**e**) The standing wave is the product of a single temporal waveform (*Wave*) and a fixed spatial profile (*Map*). The map and the waveform shown are averaged across interictal events for the example animal. (**f**) Residuals of the fit in **e** show little deviation of interictal event from standing wave. (**g**) Time course of the root mean square residuals for the standing wave model applied to interictal events (*blue*) and seizures (*red*). The spatial map was optimized to fit interictal events. Shaded areas indicate two s.e.m. (**h**) Variance explained by the standing wave model for 1 s sections of interictal events (*blue dot*) and seizures (*red dots*). Error bars show median ± 1 quartile. Shaded blue area indicates the 96% confidence interval for quality of the fit to interictal events. (**i**) Predictions of the standing wave model for the seizure in **b**. The model was imposed to have the average spatial map as interictal events, and was free to have the best fitting time course. (**j**) Residuals between seizure and standing wave model are small in the first ~0.3 s after onset, but subsequently become prominent, when the standing wave model fails to capture the propagation typical of seizures.

For interictal events, the evolution of activity in space and time was a simple standing wave: they rose and then abated while engaging a fixed spatial profile (Figure 3**d-h**). In a standing wave, the responses in all locations follow a similar time course, so that the sequence of images is the product of a single image and a single time course (Figure 3**d**-**e**). We fitted this model to the interictal events and obtained predictions that resembled closely the actual measurements (Figure 3**e**), accounting for 94±0.4% of the variance of the data (Figure 3**g**, *blue dot*). Indeed, the residuals between the data and the predictions of the model were small (Figure 3**f**), with the average residual peaking at a ΔF/F < 5% (Figure 3**h**, *blue trace*), a negligible fraction of the ΔF/F ~125% typical of interictal events.

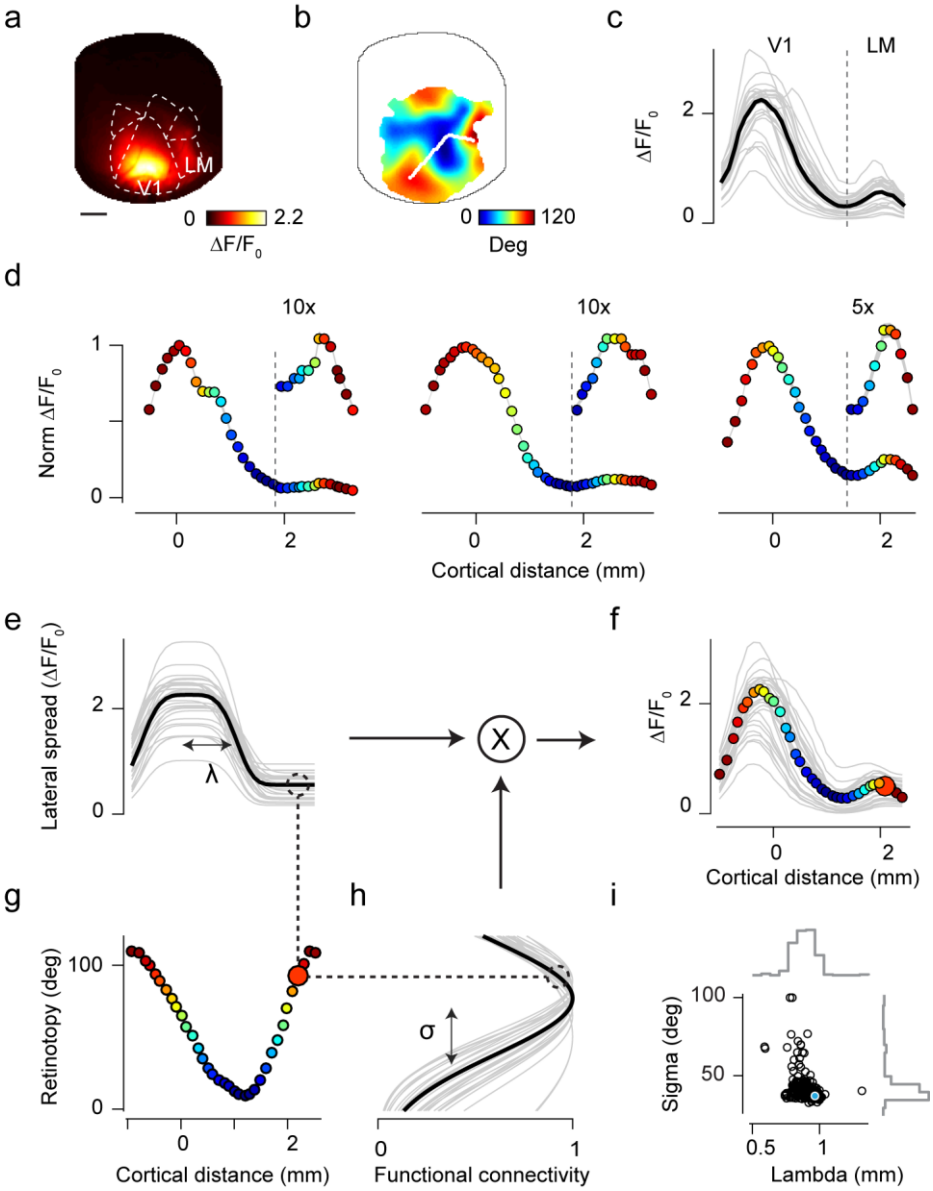

Figure 4: Interictal events and early seizures engage both lateral spread and functional connectivity. (**a**) Average spatial profile of interictal events measured in one mouse, obtained by averaging the maximum projection map across events (n = 242). Scale bar is 1 mm. (**b**) Map of retinotopy (preferred horizontal position) with a line from the focus in V1 to area LM, to join 35 regions of interest (ROIs) with same preferred vertical position as the focus in V1. (**c**) Peak dF/F response at each ROI in **b** for a representative interictal event (*black*) and for 30 other interictal events (*gray*). (**d**) The mean spatial profile across interictal events for 3 representative animals (two measured with GCaMP3 and the third with GCaMP6), where ROIs were drawn with the same strategy as in panel **b.** Dot color indicates the retinotopic preference of the corresponding ROI. Insets show the magnified profile of responses in area LM. The grey shaded line (barely visible) represents mean± s.e.m. (**e-i**) The bimodal profile of activity for each interictal event is well described by the dot product of a function of cortical distance from the focus (**e**), and a function of retinotopic distance from the focus (**h**). *Dotted lines* indicate how the model predicts the second peak of activation ~2 mm away from the focus (**f**), due to the similar retinotopic preference of that region and the focus (**g**). (**i**) Distribution of fit parameters for the example animal, indicating a consistent role of lateral spread and functional connectivity across events.

Seizures, instead, behaved as standing waves only at first, when they closely resembled interictal events, and then propagated extensively (Figure 3**h-i**). A standing wave model with the spatial profile of interictal events was appropriate to describe the beginning of the ictal events, but it became patently inadequate after a few hundred milliseconds (Figure 3**i-j**): it progressively overestimated the activity at the focus (negative residual, Figure 3**j**), while underestimating the activity in the surrounding region (positive residual, Figure 3**j**). Consequently, the quality of this model's predictions deteriorated sharply with time (Figure 3**g,h**). Seizures, thus, start as standing waves just as interictal events,

but then they progressively propagate beyond the common initial spatial profile to engage wider regions of cortex.

The common spatial profile of interictal and early ictal events typically encompassed not only the focus, but also one or more distinct regions that were homotopic, i.e. that shared the same retinotopic preferences (**Figure 4a**-**d**). For instance, two distinct lobes are clearly visible 60-100 ms into the example epileptiform events (Figure 3**a**, **c**). The first lobe lies in area V1 and the second in area LM (**Figure 4a**). To characterize these two lobes, we drew a line connecting V1 to LM along the direction of maximal change in preferred horizontal position obtained when retinotopy was mapped (**Figure 4b**). The profile of activation along this line was bimodal (**Figure 4c**), with the activation in V1 being 8±2 times higher and ~2 times wider than in LM (n = 4 mice, **Suppl. Figure 4a**-**d**). Crucially, the two activations involved regions with matching retinotopic preference (**Figure 4d**). The retinotopic preferences of the two peaks, indeed, were not significantly different (p= 0.4, Wilcoxon signed rank test), and the retinotopic preferences of the two peaks were significantly correlated (r = 0.48, p<0.001, **Suppl. Figure 4e**, **f**).

These observations indicate that two factors determine the spatial profile of interictal events and early seizures: one local, causing lateral spread and one distal, causing homotopic spread (**Figure 4e**-**i**). The local factor could, in principle, arise from disinhibition (spread of picrotoxin, loss of $GABA_A$ receptor electrochemical driving force, or depolarization block of interneurons), from local excitatory circuits, or from non-synaptic mechanisms; its impact falls off with cortical distance (**Figure 4e**). The distal factor, by contrast, arises from the same axonal and synaptic organization that supports functional connectivity, whose impact decreases with retinotopic distance (**Figure 4h**). We combined these two effects into a simple multiplicative model (**Figure 4e,g**,**h**), and found that with only 6 parameters the model provided good fits to the data (**Figure 4f**). The function of retinotopy, in particular, was described by one key parameter, the angular standard deviation σ. As this parameter grows, the function becomes closer to a constant, and retinotopy plays a lesser role in the profile of the epileptiform events. When fitting the data, σ consistently took values <40 deg (**Figure 4i**) implying an important contribution of retinotopy (**Figure 4h**), which in turn produced a clear secondary peak in activity (**Figure 4f**). Homotopic connectivity thus plays a key role in determining the spatial profile of interictal events and early seizures. Retinotopic modulation was present in all mice, but the strength of its contribution varied across animals (**Figure 4d**), possibly reflecting experimental variability in the induction of the focus and levels of expression or sensitivity of the calcium indicator.

These same two factors – lateral and homotopic – also determined the subsequent evolution of seizures, when the standing wave gave way to escalating propagation of activity (Figure 5**a**-**d**). As we have seen, seizures propagated to engage most of the visual cortex, and often beyond, producing activity levels comparable to those observed at the focus (Figure 5**a**). The pattern of propagation can be seen by following the activity of individual loci between the focus in area V1 and the homotopic location in area LM (Figure 5**b**, **c**). In the example shown, the focus in V1 had a retinotopic preference ~100 degrees away from the middle of the visual field, which is indicated in orange in the map of retinotopy (Figure 5**b**). Accordingly, at that location the calcium traces show ictal activity with the earliest onset (Figure 5**c**, *top arrow*). This activity progressively invades further V1 locations, eventually reaching the border with area LM, where receptive fields are in the middle of the visual field (0 degrees, Figure 5**c**, *blue traces*). Well before having reached those areas, however, the seizure has already reached a distal region: the portion of LM with the same retinotopic preference as the focus (Figure 5**c**, *bottom arrow*). For instance, 6 to 8 s into the event, the ictal activity shows a bimodal profile, being stronger in the homotopic regions in LM than in regions of V1 that are closer to the focus (Figure 5**d**).

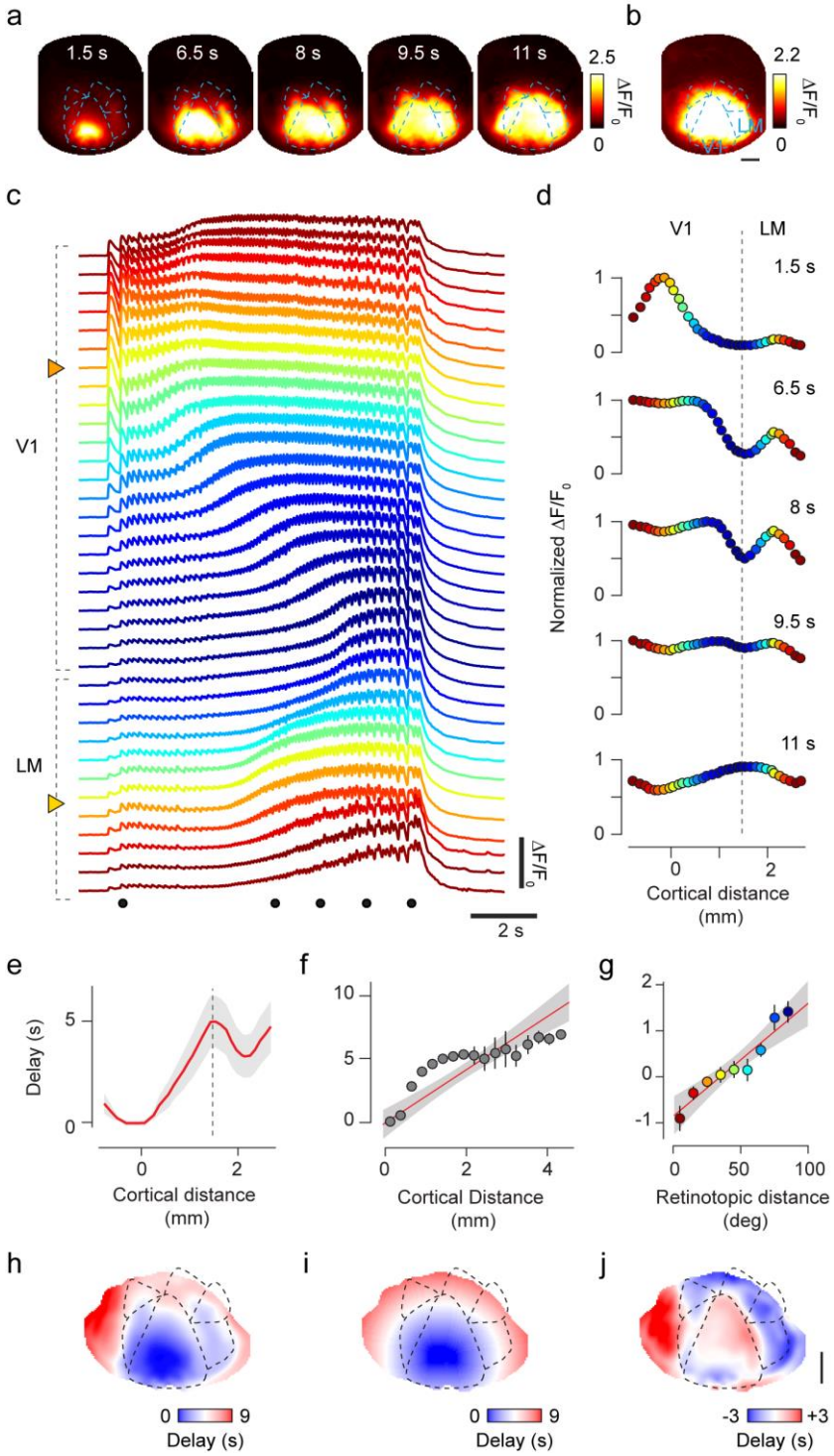

Figure 5: Seizure propagation recruits homotopic regions of cortex. (**a**) Frames obtained through GCaMP imaging in a representative seizure. Time stamps indicate time from seizure onset. (**b**) Maximum extent of seizure invasion, obtained by averaging the maximum projection map across seizures (n = 14 in one mouse). (**c**) Single trial time course along the ROIs in Figure4**b**, for the seizure in **a**. Dots mark the representative times used in **a** and **d**. Arrowheads mark the focus in V1 and secondary focus in LM. (**d**) Spatial profile of the seizure in **c**, at representative times. The traces were first normalized to their maximum. (**e**) Seizure invasion delay for each ROI, averaged across seizures. Shaded area represent s.e.m. (**f**) Dependence of seizure delay on cortical distance, averaged across animals (n=4). Error bars indicate two s.e.m. *Red line*: linear fit, with shaded 95% confidence interval. (**g**) The residuals of the linear fit in **f**, as a function of retinotopic distance from the focus. *Red line*: linear fit, with shaded 95% confidence interval. (**h**) Map of delay to seizure invasion, averaged across seizures (n=14 in one mouse). (**i**) Prediction of that map based solely on cortical distance from the focus. (**j**) Residuals of that prediction. Scale bars are 1 mm.

The two factors, lateral and homotopic, both contributed approximately linearly to the time course of seizure propagation (Figure 5**e**-**j**). To measure the time it took for a seizure to invade each pixel, we defined a 'delay to seizure invasion' as the time taken for the pixel to reach 60% of its maximum activity. Consistent with the observations made above, a map of this quantity shows activations occurring earlier in the V1 focus and in the homotopic region in LM than in other locations (Figure 5**h**) and a plot of delay along a line from V1 to LM shows delay growing with distance while displaying two distinct troughs (Figure 5**e**). When averaging these measures across mice, we found that delay strongly correlated with distance ($r = 0.81$, $p < 10^{-7}$, $n = 64$ seizures in 4 mice), with an average propagation speed of 0.48 ± 0.03 mm/s (Figure 5**f**). However, closer inspection of this linear prediction based on distance shows that it underestimates the delays of proximal territories and overestimates those of distal territories (Figure 5**f**). The corresponding residuals were highly correlated with retinotopic distance from the focus ($r = 0.82$, $p < 10^{-24}$, Figure 5**g**). Indeed, if delay to cortical invasion were solely due to cortical distance, it would grow radially from the focus and display concentric rings (Figure 5**i**). The map of residuals instead reveals that it underestimates delays in territories retinotopically close to the focus, especially in higher visual areas (Figure 5**j**, *blue negative residual*), and overestimates delays in distal territories in V1 and in regions outside the visual areas (Figure 5**j**, *red positive residual*). These results indicate that delay to ictal invasion depends approximately linearly on two factors: one lateral, which grows with distance in cortex, and one homotopic, which grows with distance in visual preference.

Homotopic factors also played a key role in the timing of the prominent individual oscillatory waves of activity seen during seizures (Figure 6). Once a territory was invaded by seizure activity, it displayed striking fast oscillations in the range of 6-11 Hz, evident both in the LFP and in the GCaMP fluorescence (Figure 6**a, c** , Figure 5**a** , Suppl. Figure 3**a**). These oscillations continued until the seizure spread to the entire visual cortex and beyond, after which we occasionally observed more diverse patterns (such as spiral waves[34,35]). To isolate the fast oscillations from the slow spreading activity, we filtered the traces in that frequency range, and used the Hilbert Transform to compute the amplitude and phase of the oscillation for the LFP and for each pixel at each time point (Figure 6**a, c**) . During an epoch starting 3.4±0.1 s after seizure initiation and lasting 3.7±0.8 s (Figure 6**a, c**), the seizure focus acted as a pacemaker for the oscillations: each oscillatory wave started at the focus and propagated on the surface of the cortex. The spatiotemporal pattern of these oscillations was highly stereotypic (Figure 6**b**, **d**): the map of their delay was consistent across oscillations (Figure 6**c**) and closely related to the map of retinotopy (Figure 6**b**). Accordingly, the average oscillation shows activity progressively entraining a larger region of cortex, propagating homotopically like the slow wave of seizure recruitment (Suppl**. Movie 3**). Similar results were seen in other mice: in all cycles the LFP and GCaMP signatures of the oscillations were consistent (Figure 6**g, h, m**) and maps of delay were strikingly similar to the retinotopic maps (Figure 6**d**-**g**). Just like the slow spread of seizure activity, therefore, the fast oscillations that characterize this activity propagate along the same functional circuits that support neural signals during normal cortical activity.

Discussion

By exploiting the potential of widefield imaging and of genetically encoded calcium indicators, we were able to study the spatiotemporal evolution of epileptiform activity in the awake cortex and relate this evolution to the underlying functional architecture. Focal picrotoxin injections induced prolonged seizures with clear behavioral correlates, separated by numerous brief interictal events. In the first few hundred milliseconds from their onset, the two types of discharge were extremely similar: they were standing waves of activity with a fixed spatial profile. Afterwards, however, interictal events subsided while seizures went on to invade much of visual cortex and beyond. Individual fast waves of activity within seizures also spread in a similar manner.

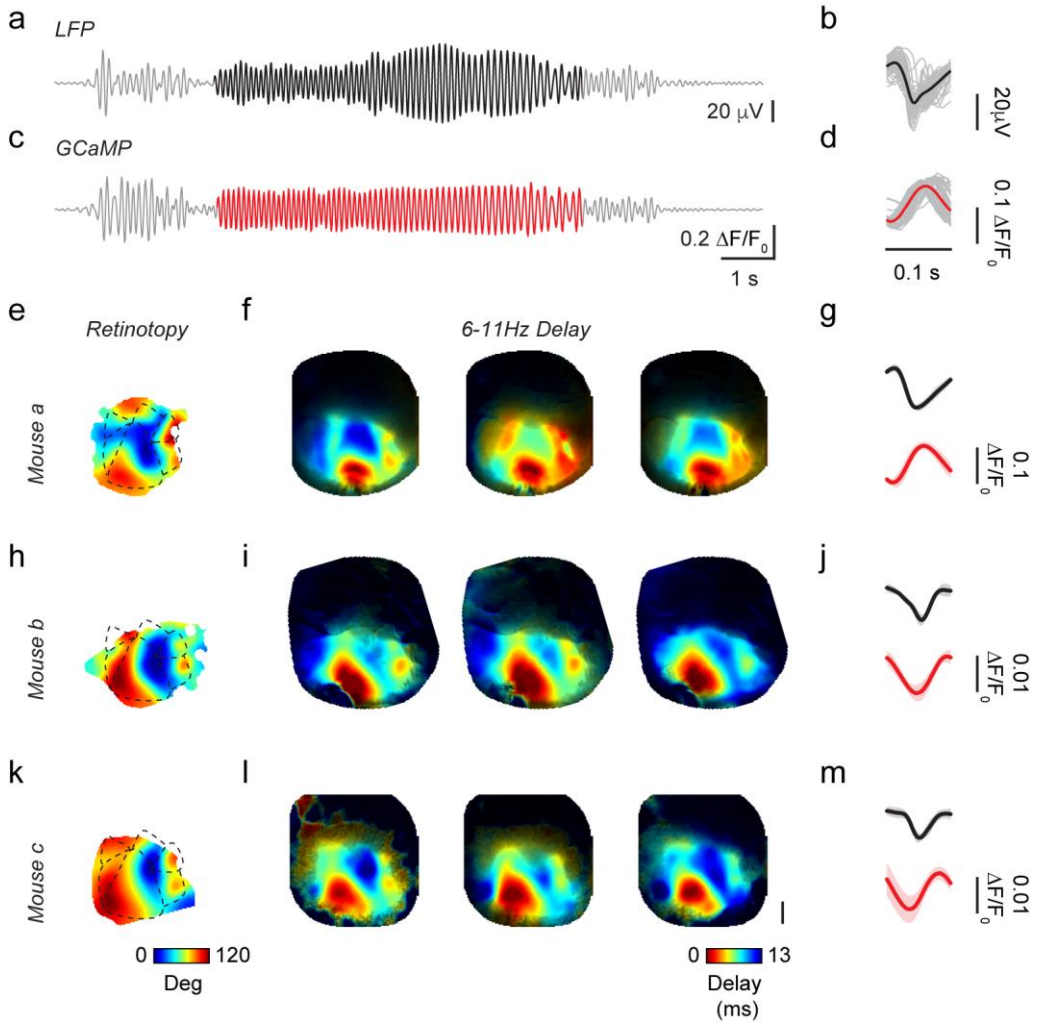

Figure 6: Homotopic propagation of fast oscillations during seizures. (**a**) LFP recording of seizure, bandpass filtered between 6-11 Hz, same example seizure as in Figure 5**a**. Highlighted in black is the epoch of coherent oscillations driven by the focus, used for the analysis in the next panels. (**b**) Cycle average of the 6-11 Hz oscillation from the unfiltered LFP trace. Gray traces show the individual cycles of the oscillation. (**c**, **d**) Same as **a, b**, for the GCaMP fluorescence measured at the focus. Oscillation highlighted in red. (**e**) Retinotopic maps for an example animal. (**f**) Delay to invasion of fast oscillations for three example seizures from this example animal. Delay was obtained from the 6-11 Hz Hilbert phase referenced at the focus, averaged across all cycles of the oscillation for a given seizure. (**g**) Average LFP cycle (*top*) and average GCaMP fluorescence (*bottom*), averaged across all the seizures for this animal. Shaded area represent the standard deviation. (**h**-**m**) Same as **e**-**g** for six other seizures in two other mice. In all seizures and all mice, the delay of the fast oscillation faithfully recapitulates the retinotopic maps. Scale bar 1 mm.

Strikingly, all of these epileptiform phenomena respected the functional connectivity of the visual cortex observed during normal sensory processing. Specifically, the phenomena were shaped by a combination of two factors, one local and dependent on cortical distance from the focus, and one distal and dependent on homotopic relationship with the focus. Both factors determined the shape of the common spatial footprint characteristic of interictal events and of seizure onset (Figure 4). Both factors determined the slow spread of the seizures (Figure 5). Both factors also determined the fast spread of the prominent oscillations that accompany the seizures (Figure 6).

These local and distal factors likely reflect different mechanisms. Distal propagation must rely on synaptic barrages transmitted from the seizure focus through long-range, excitatory pathways connecting homotopic regions. Local propagation, in addition, can involve collapse of local inhibition [12,13], although evidence exists for a host of non-synaptic mechanisms such as gap junctions among neurons [11] or astrocytes [10], alterations

in the electrochemical gradients of chloride [8,9] or potassium [7], endogenous electric fields [5,6] and defective astrocyte calcium signaling [4].

The combination of widefield imaging and genetically encoded calcium indicators represents a substantial advance over electrophysiological recordings performed at a few sites[36,3738], and complements the measures that can be obtained with high-density electrode arrays[12]. Widefield imaging has long been recognized as a promising alternative, and has been applied to measure hemodynamic signals[3,39],voltage-sensitive fluorescent dyes[40], or organic calcium dyes [41]. These techniques, however, provide much weaker signals than genetically encoded calcium indicators. These indicators can be targeted to specific types of neurons, have high signal to noise ratios and provide a faithful representation of the underlying neural activity, with appropriate spatial and temporal resolution[28,26,42]. Indeed, the signal to noise ratio of the calcium indicators used here allowed single trial analysis without the need to average responses. Recording in awake animals, moreover, avoided the confounding effects of anesthesia.

These differences in methods may explain a difference between our results and those of earlier studies. Whereas we found a strong relationship between the propagation of epileptiform activity and the underlying functional architecture, previous widefield imaging studies found only a weak relationship[40] or no relationship[3,39]. In addition to the choice of indicators, these differences could be easily due to differences in the neural systems under study. For instance, it is likely that the functional connectivity between two regions having the same retinotopic preference across visual areas is stronger than the connectivity between two regions having the same orientation preference within area V1.

We did not observe decreases in fluorescence in regions surrounding epileptiform activity, as one might have expected from an “inhibitory surround” [19]. This finding may seem to be in contradiction with an earlier study of hemodynamic signals, which were found to be decreased in the region around the focus[3]. Neither our study nor the previous study, however, employed the ideal methods to probe inhibition. Indeed, decreases in hemodynamic signals cannot be interpreted as increases in inhibition, because: interneuron activation has the opposite effect[43]. Our methods, likewise, are not ideal to study inhibition: we measured calcium signals only in excitatory neurons, and these signals reflect mostly supra-threshold activity and may be insensitive to hyperpolarization below threshold. The question of what interneurons do in the region surrounding the focus thus remains open and can be addressed in future studies by genetically targeting those neurons for widefield imaging.

The striking similarity that we found between interictal events and the onset of seizures suggests that the two are mechanistically related. Interictal events have long been recognized as an electrophysiological marker of epilepsy [16], but have no or only subtle clinical correlates[44]. They have been proposed either to prevent seizure initiation [18]or to act as a prelude to seizures[45]. It has, furthermore, been proposed that interictal events dominated by GABAergic signaling give way to glutamatergic pre-ictal events [20]. Our results do not reveal any detectable differences between interictal events and seizures during the first few hundred milliseconds: both are well modeled as standing waves involving the same temporal profile over a fixed spatial territory. It remains to be determined whether a qualitative or quantitative difference in the underlying cellular mechanisms lead to these events dying down (and thus become interictal) or turning into propagating seizures. A plausible distinction is that seizures result from escape from an inhibitory restraint[46]. Indeed, the smaller peak of activity in LM during interictal discharges is consistent with a barrage of feed-forward activity that fails to recruit a self-sustaining discharge. To test this hypothesis, once again, it would be useful to express the calcium indicator in inhibitory neurons and compare their activity in interictal events and seizures.

The seizures induced in our preparation bear numerous similarities with seizures observed in patients. Their speed of propagation across the cortex, ~0.5 mm/s, is consistent with measurements obtained with high-density electrode arrays from seizures recorded in

humans with cortical epilepsy[12]. However, propagation to LM is consistent with recruitment of more distant areas at short latency. Moreover, our results demonstrate that cortico-cortical connections that support higher visual processing have an important role in determining the propagation of seizures originating in V1. The involvement of higher-order visual cortex is consistent with seizures seen in occipital epilepsy, which commonly includes both elemental symptoms in specific areas of the visual field and more complex visual hallucinations[47], which might be expected from the engagement of higher visual areas.

Our characterization of the spatiotemporal flow of activity in epileptic discharges provides a platform for further understanding the mechanisms of epilepsy and for testing therapeutic approaches. In particular, the techniques and results introduced here may help shed light on the mechanisms of secondary generalization of partial-onset seizures. Secondary generalization sharply reduces the efficacy of surgical removal of the primary lesion[48] and is thus a hallmark of refractory epilepsy, with substantial impact on quality of life and increased risk of mortality[49,50]. Although secondary generalization ultimately involves subcortical structures[2] it is commonly preceded by invasion of neighboring regions of cortex[51]. The techniques introduced here may make this process amenable to study, and may provide a benchmark to identify and test novel therapeutic targets.

Acknowledgements

We thank Michael Okun and Daisuke Shimaoka for assistance in experimental setup and data analysis, and Charu Reddy for animal husbandry and histology. This work was supported by the Wellcome Trust (095669-Z-11-Z) and Epilepsy Research UK. L.F.R. was funded by the Wellcome Trust PhD programme in Neuroscience at UCL. M.C. holds the GlaxoSmithKline/Fight for Sight Chair in Visual Neuroscience.

Methods

All experimental procedures were conducted according to the UK Animals Scientific Procedures Act (1986). Experiments were performed at University College London, under personal and project licenses released by the Home Office following appropriate ethics review.

All data analysis was performed in MATLAB (The MathWorks Inc.).

Transgenic lines

Emx1::Cre-flex-GCaMP3 mice were generated by crossing the following two transgenic lines: Emx1-IRES-Cre, expressing Cre recombinase under the Emx1 promoter (catalog #005628, The Jackson Laboratory); and a reporter Ai38-GCaMP3 line (catalog #014538, The Jackson Laboratory), carrying a floxed copy of the GCaMP3 gene under the strong CAG promoter in the Rosa26 locus. Offspring expressed GCaMP3 in excitatory neurons of the neocortex and hippocampus [29,25].

Rasgrf-dCre-CaMKIIa-TTA-TITL-GCaMP6f triple transgenics[28] were generated by breeding Rasgrf-dCre, CamKII-tta and Ai93(TITL-GCaMP6f) mice. Three weeks before imaging, TMP was orally administered for 3 consecutive days to trigger dCre-mediated recombination. With this system, flex-GCaMP6f recombination was induced only in Rasgrf positive neurons, while transcription was further restricted to CaMKIIa expressing neurons that also expressed the transcription factor TTA. As a result, GCaMP6 expression was selective to pyramidal neurons located in layers 2/3 and sparsely in layer 5.

Although GCaMP6f allows for the detection of population activity with higher signal to noise ratio than GCaMP3, the cortical activations studied here were so massive that this made little difference. We thus present data obtained with both indicators.

Surgical procedures

Using aseptic techniques, animals were chronically implanted with a thinned skull cranial window under isoflurane anesthesia. 0.05mL Rimadyl (Carprofen 5%

w/v) was administered before surgery as an anti-inflammatory and analgesic. During the procedure, eyes were protected with ophthalmic gel (Viscotears Liquid Gel, Alcan) and the body temperature maintained around 37°C. The animal was anesthetized and mounted in a stereotaxic frame. The scalp over the dorsal skull surface was removed to expose the cranium. The left hemisphere parietal bone was thinned using a scalpel blade. Thinning proceeded until the cancellous layer of the skull, which contains blood vessels, was completely removed. A custom-made stainless steel head plate with a round imaging chamber (8 mm diameter) was then cemented over the thinned area using dental cement (Superbond). Finally, a small drop of UV cement (Norland Products Inc.) was applied inside the imaging chamber and an 8 mm glass coverslip glued onto the thinned skull region. The cement was cured with an UV LED (390nm, ThorLabs) for 20 s. The animal was allowed to recover at 37°C in an incubator and provided with Rimadyl in the drinking water (0.1 mL in 100 mL) for the three days after the surgery.

On the day of LFP recordings, the animal was anaesthetized again and a small skull screw implanted in the contralateral frontal bone, rostral to the cranial window. A silver wire previously soldered to the screw head served as a reference for electrophysiological recordings. After opening a small hole in the cranial window coverslip, a small craniotomy was performed over the target region of V1. The exposed region was finally covered with KwicKast silicone elastomer sealant. The animal was allowed to fully recover before starting the recording session. The typical recording session of epileptiform activity lasted 30-40 minutes.

Visual stimulation and retinotopic mapping

Visual stimuli were presented on three LCD monitors[26], positioned 30 cm from the animal, arranged to span 140 degrees in azimuth and 60 degrees in elevation of the visual field contralateral to the imaged hemisphere. For retinotopic mapping, stimuli were contrast-reversing gratings presented inside a rectangular window. Stimulus duration was 5 s, flickering frequency was 2 Hz, and spatial frequency was 0.03 cycles/°. To measure the preferred azimuth, the rectangular window was 60° high and 30° wide. To measure the preferred elevation, it was 20° high and 140° wide. Eye movements were monitored with CCD camera equipped with 2 infrared LEDs.

Electrophysiology

Local field potential (LFP) was recorded with Ag-Cl electrodes in ACSF-filled borosilicate micropipettes (typical tip aperture 2-3 µm, 1-3 MΩ). To induce epileptiform activity, 10 mM Picrotoxin (Sigma) dissolved in DMSO (Sigma) was added to the recording solution. During these experiments, the pipette was pushed through the dura without applying pressure, to avoid injection of the GABAergic antagonist. The pressure inside the pipette was measured with a differential manometer. The resistance of the micropipette was monitored to ensure that insertion in the brain didn't clog the tip.

LFP signals were amplified 1,000 fold and high-passed above 0.1 Hz via a Multiclamp 700B differential amplifier (Molecular Devices). Data were digitized at 10 kHz with a Blackrock acquisition system and software. The exposure signal from the camera, TTL signals from visual stimulation software and screen photodiode signal were recorded at the same time to synchronize electrophysiological, imaging and visual stimulation data.

LFP analysis

To identify the start times of interictal discharges and seizures from the LFP recording we devised a simple supervised event detection method. The LFP trace was resampled at 100 Hz; the start of each event was assigned to the local maxima of the first derivative of the signal that exceeded 3 standard deviations from baseline; the end of each discharge was identified when its low frequency envelope returned to baseline. Finally, the results of the automatic detection were inspected visually and events classified as interictal discharges or seizures. Missed events were manually selected and artifacts removed.

Wavelet scalograms of the LFP signal were computed using the wavelet toolbox provided by Torrence and Compo (atoc.colorado.edu/research/wavelets). Power

spectra and coherence of LFP and fluorescence signals were calculated using the Chronux Toolbox[52] (http://chronux.org/).

Widefield calcium imaging

We recorded GCaMP fluorescence with an epi-illumination system[26]. Excitation light at 480nm was provided with a blue LED light (465nm LEX2-B, Brain Vision, band-passed with a Semrock FF01-482/35 filter) and diverted onto the visual cortex via a dichroic mirror (FF506-Di03, Semrock). The emitted fluorescence was reflected by a second dichroic mirror (FF593-Di03, Semrock), passed through an emission filter (FF01-543/50-25, Semrock), and collected by a sCMOS camera (pco.edge, PCO AG). The camera was controlled by a TTL external trigger synchronized with the visual stimulation. The image acquisition rate was 50 Hz for retinotopic mapping and 70 Hz during imaging of epileptiform activity. The nominal spatial resolution of the system was 200 pixel/mm. Imaging was conducted in 20 s long sweeps, interleaved with ~10 s pauses needed to save the data to disk.

Histology and confocal imaging

To prepare the brain for tissue section, the animal was anesthetized (pentobarbital sodium, 200 mg/kg, i.p.), and the heart was perfused with PBS (0.5 ml/min) followed by a fixative (paraformaldehyde, 4%) in PBS solution. The brain was then removed and immersed in a PBS containing 30% sucrose at 4°C. Frozen coronal sections (60 µm thick) were obtained with a sliding microtome (Microm HM400R), mounted on glass slides and stained with DAPI (Vectashield). Sections were later imaged through a confocal microscope (Zeiss).

Analysis of imaging movies

Widefield movies where first registered using a discrete Fourier transform based subpixel image registration algorithm[53]. The retinotopic mapping and epileptiform activity images where then aligned using the brain vasculature as a reference. Affine transformation was used to find the best alignment. Then we calculated $\Delta F/F_0$ movies, where the signal for each pixel x was obtained as

$$\frac{\Delta F(t,x)}{F_0(x)} = \frac{F(t,x) - F_0(x)}{F_0(x)}$$

F_0 was computed as the 20th percentile of each imaging sweep. Finally, a mask was manually drawn to segment out the visible cortex form the edges of the implant.

The map of retinotopy was obtained as previously described[26] In short, the reversing gratings elicited periodic neural responses that oscillate at twice the frequency of reversal[54]. For each pixel, we measured the power of these second harmonic responses using the Fourier transform of the fluorescent trace. We then fitted a Gaussian position tuning curve to the amplitude of the responses to visual stimulation at four horizontal positions. The standard deviation for the Gaussian curve model was the one that minimized the least squared error of the fit across pixels.

To localize the cortical initiation site of each event, calcium signals were aligned by the start of the electrographic discharge. For each event, pixels were included if they showed ΔF/F increases greater than 60% of the peak ΔF/F reached in the same class of events. The center of mass of the resulting cortical area, calculated over the first 500 ms, was then taken as the site of initiation of epileptiform activity. The average retinotopic position of the focus across animals was 93±16 degrees, confirming our ability to target the medial region of V1. We restricted the analysis to events that where contained for the most part in an imaging sweep. In particular, we included seizures that where imaged for at least 6 s after their start.

To assess the slow propagation of seizures, we defined criteria to evaluate when a cortical territory was invaded by the seizing activity. The distribution of maximum florescence levels during seizure was bimodal (Suppl. Figure 5). We considered recruited to the seizure the pixels that exceeded 30% of the peak fluorescence recorded at the focus, which was a good threshold to separate the population of pixels with the highest fluorescence change (Suppl. Figure 5). We then calculated the time it took for a seizure to invade each recruited pixel, measured from the electrographic seizure onset. We called this time 'delay to seizure invasion', and we measured it as the time point at which

the fluorescence at any recruited pixel reached 60% of its maximum.

Standing wave model

We modeled the fluorescence movies of epileptiform discharges as standing waves, i.e. as the product of a global time course and a single image.

$$Movie = Timecourse * Map + Residual$$

To find the best standing wave approximation, we applied singular value decomposition (SVD), a matrix factorization algorithm. SVD returns the best least square approximation of a matrix as the sum of standing waves. We obtained the time course and map of the separable model from the first row and first column returned by the SVD factorization.

Modelling of the profile of interictal events

We modeled the retinotopic profile of activation elicited by interictal events as the dot product of two functions, both dependent on the cortical position **x** of each ROI.

The first function depends on functional connectivity, and is a Gaussian falling off with the retinotopic distance from the focus, *ret(**x**)*:

$$FC(\boldsymbol{x}) = e^{\frac{-(ret(\boldsymbol{x}) - ret_{focus})^2}{2\sigma^2}}$$

The second function depends on lateral spread, and is a Gaussian-like function with the numerator raised to the 4th power to give it a flat top as it falls off with the cortical distance from the epileptic focus:

$$LS(\boldsymbol{x}) = (A - B)e^{\frac{-abs(\boldsymbol{x} - x_{focus})^4}{\lambda^4/ln(2)}} + B$$

When so parametrized, λ corresponds to the half-width half-maximum of the function. We fitted the parameters σ, λ, ret_{focus}, x_{focus} ,A, B to the data by least square minimization.

Phase analysis of cortical oscillations

Movies of cortical seizures were first bandpass filtered between 6 and 11 Hz. Then we computed the analytical representation of the fluorescence time-course for each pixel, using the Hilbert transform (MATLAB function 'hilbert', Signal Processing Toolbox). The analytical signal $S_a(t)$ is a representation of a real valued signal $f(t)$ in the complex space:

$$S_a(t) = f(t) + iH(f)(t) = A(t)e^{i\varphi(t)}$$

Its real part is $f(t)$, the fluorescence signal, while its imaginary part is $H(f)(t)$, the Hilbert transform of $f(t)$. When expressed in polar form, the analytical signal $S_a(t)$ has a straightforward interpretation: the modulus $A(t)$ represents the instantaneous amplitude, or envelope, of the oscillation; the angle $\varphi(t)$ represents the instantaneous phase of the oscillation.

Statistical information

Data were tested for normality before choosing the appropriate statistical test. All the statistical tests used were 2 tailed test. The significance of linear regression models was tested with the F-statistic against the null hypothesis of a constant model. p = 0.05 was assumed as the threshold for statistical significance.

References

1. Wiebe, S. & Jette, N. Pharmacoresistance and the role of surgery in difficult to treat epilepsy. *Nat. Rev. Neurol.* **8,** 669–677 (2012).

2. Motelow, J. E. *et al.* Decreased subcortical cholinergic arousal in focal seizures. *Neuron* **85,** 561–572 (2015).

3. Schwartz, T. H. & Bonhoeffer, T. In vivo optical mapping of epileptic foci and surround inhibition in ferret cerebral cortex. *Nat. Med.* **7,** 1063–7 (2001).

4. Carmignoto, G. & Haydon, P. G. Astrocyte calcium signaling and epilepsy. *Glia* **60,** 1227–1233 (2012).

5. Qiu, C., Shivacharan, R. S., Zhang, M. & Durand, D. M. Can Neural Activity Propagate by Endogenous Electrical Field? *J. Neurosci.* **35,** 15800–15811 (2015).

6. Zhang, M. *et al.* Propagation of epileptiform activity can be independent of synaptic transmission, gap junctions, or diffusion and is consistent with electrical field transmission. *J. Neurosci.* **34,** 1409–1419 (2014).

7. Voipio, J. & Kaila, K. GABAergic excitation and K+-mediated volume transmission in the hippocampus. *Prog. Brain Res.* **125,** 329–338 (2000).

8. Staley, K. J., Soldo, B. L. & Proctor, W. R. Ionic mechanisms of neuronal excitation by inhibitory GABAA receptors. *Sci. (New York, NY)* **269,** 977–981 (1995).

9. Huberfeld, G. *et al.* Perturbed chloride homeostasis and GABAergic signaling in human temporal lobe epilepsy. *J. Neurosci.* **27,** 9866–9873 (2007).

10. Bedner, P. *et al.* Astrocyte uncoupling as a cause of human temporal lobe epilepsy. *Brain* **138,** 1208–1222 (2015).

11. Gyengesi, G. Z., Hermesz, E., Ks, A. & Szente M. Involvement of Gap Junctions in the Manifestation and Control of the Duration of Seizures in Rats In Vivo. *Epilepsia* **44,** 1596–1600 (2003).

12. Schevon, C. a *et al.* Evidence of an inhibitory restraint of seizure activity in humans. *Nat. Commun.* **3,** 1060 (2012).

13. Trevelyan, A. J., Sussillo, D. & Yuste, R. Feedforward inhibition contributes to the control of epileptiform propagation speed. *J. Neurosci.* **27,** 3383–7 (2007).

14. Goodkin, H. P. Status Epilepticus Increases the Intracellular Accumulation of GABAA Receptors. *J. Neurosci.* **25,** 5511–5520 (2005).

15. Ziburkus, J., Cressman, J. R., Barreto, E. & Schiff, S. J. Interneuron and pyramidal cell interplay during in vitro seizure-like events. *J. Neurophysiol.* **95,** 3948–54 (2006).

16. Muldoon, S. F. *et al.* GABAergic inhibition shapes interictal dynamics in awake epileptic mice. *Brain* **138,** 2875–2890 (2015).

17. Smith, E. H. *et al.* The ictal wavefront is the spatiotemporal source of discharges during spontaneous human seizures. *Nat. Commun.* **7,** 11098 (2016).

18. De Curtis, M. & Avanzini, G. Interictal spikes in focal epileptogenesis. *Prog. Neurobiol.* **63,** 541–567 (2001).

19. Prince, D. A. & Wilder, B. J. Control Mechanisms of Cortical Epileptogenic Foci. (1967).

20. Huberfeld, G. *et al.* Glutamatergic pre-ictal discharges emerge at the transition to seizure in human epilepsy. *Nat. Neurosci.* **14,** 627–34 (2011).

21. Garrett, M. E., Nauhaus, I., Marshel, J. H. & Callaway, X. E. M. Topography and Areal Organization of Mouse Visual Cortex. *J. Neurosci.* **34,** 12587–12600 (2014).

22. Andermann, M. L., Kerlin, A. M., Roumis, D. K., Glickfeld, L. L. & Reid, R. C. Functional specialization of mouse higher visual cortical areas. *Neuron* **72,** 1025–39 (2011).

23. Wang, Q. & Burkhalter, A. Area Map of Mouse Visual Cortex. **357,** 339–357 (2007).

24. Glickfeld, L. L., Andermann, M. L., Bonin, V. & Reid, R. C. Cortico-cortical projections in mouse visual cortex are functionally target specific. *Nat. Neurosci.* **16,** 219–26 (2013).

25. Vanni, M. P. & Murphy, T. H. Mesoscale Transcranial Spontaneous Activity Mapping in GCaMP3 Transgenic Mice Reveals Extensive Reciprocal Connections between Areas of Somatomotor Cortex. *J. Neurosci.* **34,** 15931–15946 (2014).

26. Carandini, M. *et al.* Imaging the Awake Visual Cortex with a Genetically Encoded Voltage Indicator. *J. Neurosci.* **35,** 53–63 (2015).

27. Zariwala, H. A. *et al.* A Cre-dependent GCaMP3 reporter mouse for neuronal imaging in vivo. *J Neurosci* **32,** 3131–3141 (2012).

28. Madisen, L. *et al.* Transgenic Mice for Intersectional Targeting of Neural Sensors and Effectors with High Specificity and Performance. *Neuron* **85,** 942–958 (2015).

29. Gorski, J. a *et al.* Cortical excitatory neurons and glia, but not GABAergic neurons, are produced in the Emx1-expressing lineage. *J. Neurosci.* **22,** 6309–14 (2002).

30. Andermann, M. L., Kerlin, A. M., Roumis, D. K., Glickfeld, L. L. & Reid, R. C. Functional specialization of mouse higher visual cortical areas. *Neuron* **72,** 1025–39 (2011).

31. Polack, P.-O. & Contreras, D. Long-range parallel processing and local recurrent activity in the visual cortex of the mouse. *J. Neurosci.* **32,** 11120–31 (2012).

32. Beltramo, R. *et al.* Layer-specific excitatory circuits differentially control recurrent network dynamics in the neocortex. *Nat. Neurosci.* **16,** 227–34 (2013).

33. Wekselblatt, J. B., Flister, E. D., Piscopo, D. M. & Niell, C. M. Large-scale imaging of cortical dynamics during sensory perception and behavior. *J. Neurophysiol.* jn.01056.2015 (2016). doi:10.1152/jn.01056.2015

34. Huang, X. *et al.* Spiral Wave Dynamics in Neocortex. *Neuron* **68,** 978–990 (2010).

35. Viventi, J. *et al.* Flexible, foldable, actively multiplexed, high-density electrode array for mapping brain activity in vivo. *Nat. Neurosci.* **14,** 1599–1605 (2011).

36. Wadman, W. J. & Gutnick, M. J. Non-uniform propagation of epileptiform discharge in brain slices of rat neocortex. *Neuroscience* **52,** 255–262 (1993).

37. Chervin, R. D., Pierce, P. a & Connors, B. W. Periodicity and directionality in the propagation of epileptiform discharges across neocortex. *J. Neurophysiol.* **60,** 1695–1713 (1988).

38. Goldensohn, E. S., Zablow, L. & Salazar, A. The penicillin focus. I. Distribution of potential at the cortical surface. *Electroencephalogr. Clin. Neurophysiol.* **42,** 480–492 (1977).

39. Schwartz, T. H. Optical Imaging of Epileptiform Events in Visual Cortex in Response to Patterned Photic Stimulation. *Cereb. Cortex* **13,** 1287–1298 (2003).

40. Haglund, M. M. Optical imaging of visual cortex epileptic foci and propagation pathways. *Epilepsia* **53,** 87–97 (2012).

41. Daniel, A. G. S., Laffont, P., Zhao, M., Ma, H. & Schwartz, T. H. Optical electrocorticogram (OECoG) using widefield calcium imaging reveals the divergence of neuronal and glial activity during acute rodent seizures. *Epilepsy Behav.* **49,** 61–65 (2015).

42. Chen, T.-W. *et al.* Ultrasensitive fluorescent proteins for imaging neuronal activity. *Nature* **499,** 295–300 (2013).

43. Anenberg, E., Chan, A. W., Xie, Y., LeDue, J. M. & Murphy, T. H. Optogenetic stimulation of GABA neurons can decrease local neuronal activity while increasing cortical blood flow. *J. Cereb. Blood Flow Metab.* **35,** 1579–86 (2015).

44. Kleen, J. K. *et al.* Hippocampal interictal epileptiform activity disrupts cognition in humans. *Neurology* **81,** 18–24 (2013).

45. Staley, K. J., White, A. & Dudek, F. E. Interictal spikes: Harbingers or causes of epilepsy? *Neurosci. Lett.* **497,** 247–250 (2011).

46. Trevelyan, A. J., Sussillo, D., Watson, B. O. & Yuste, R. Modular propagation of epileptiform activity: evidence for an inhibitory veto in neocortex. *J. Neurosci.* **26,** 12447–55 (2006).

47. Blume, W. T., Wiebe, S. & Tapsell, L. M. Occipital epilepsy: Lateral versus mesial. *Brain* **128,** 1209–1225 (2005).

48. Cendes, F. *et al.* Frequency and characteristics of dual pathology in patients with lesional epilepsy. *Neurology* **45,** 2058–2064 (1995).

49. Walczak, T. S. *et al.* Incidence and risk factors in sudden unexpected death in epilepsy: a prospective cohort study. *Neurology* **56,** 519–525 (2001).

50. Lawn, N. D., Bamlet, W. R., Radhakrishnan, K., O'Brien, P. C. & So, E. L. Injuries due to seizures in persons with epilepsy: A population-based study. *Neurology* **63,** 1565–1570 (2004).

51. Yoo, J. Y. *et al.* Ictal spread of medial temporal lobe seizures with and without secondary generalization: An intracranial electroencephalography analysis. *Epilepsia* **55,** 289–295 (2014).

52. Mitra, P. & Bokil, H. *Observed Brain Dynamics*. *Oxoford University Press, New York* (2008). doi:10.1093/acprof:oso/9780195178081.001.0001

53. Guizar-Sicairos, M., Thurman, S. T. & Fienup, J. R. Efficient subpixel image registration algorithms. *Opt. Lett.* **33,** 156–158 (2008).

54. Benucci, A., Frazor, R. a & Carandini, M. Standing waves and traveling waves distinguish two circuits in visual cortex. *Neuron* **55,** 103–17 (2007).

Supplementary figures

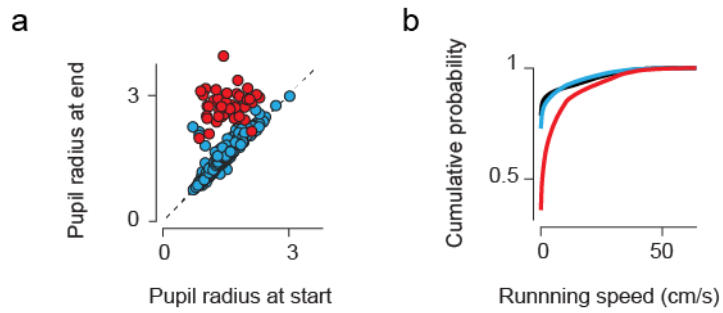

Suppl. Figure 1 Behavioral correlates of epileptiform discharges. (**a**) Relationship between pupil dilation at the start (abscissa) and at the end (ordinate) of epileptic discharges of the two types (**437** interictal events and **47** seizures from 2 animals). (**b**) Cumulative distribution of running speed in a 2 s window following the onset of interictal events (blue) and during seizures (orange), compared to baseline measurements obtained between events (black). Data normalized and averaged across **5 a**nimals.

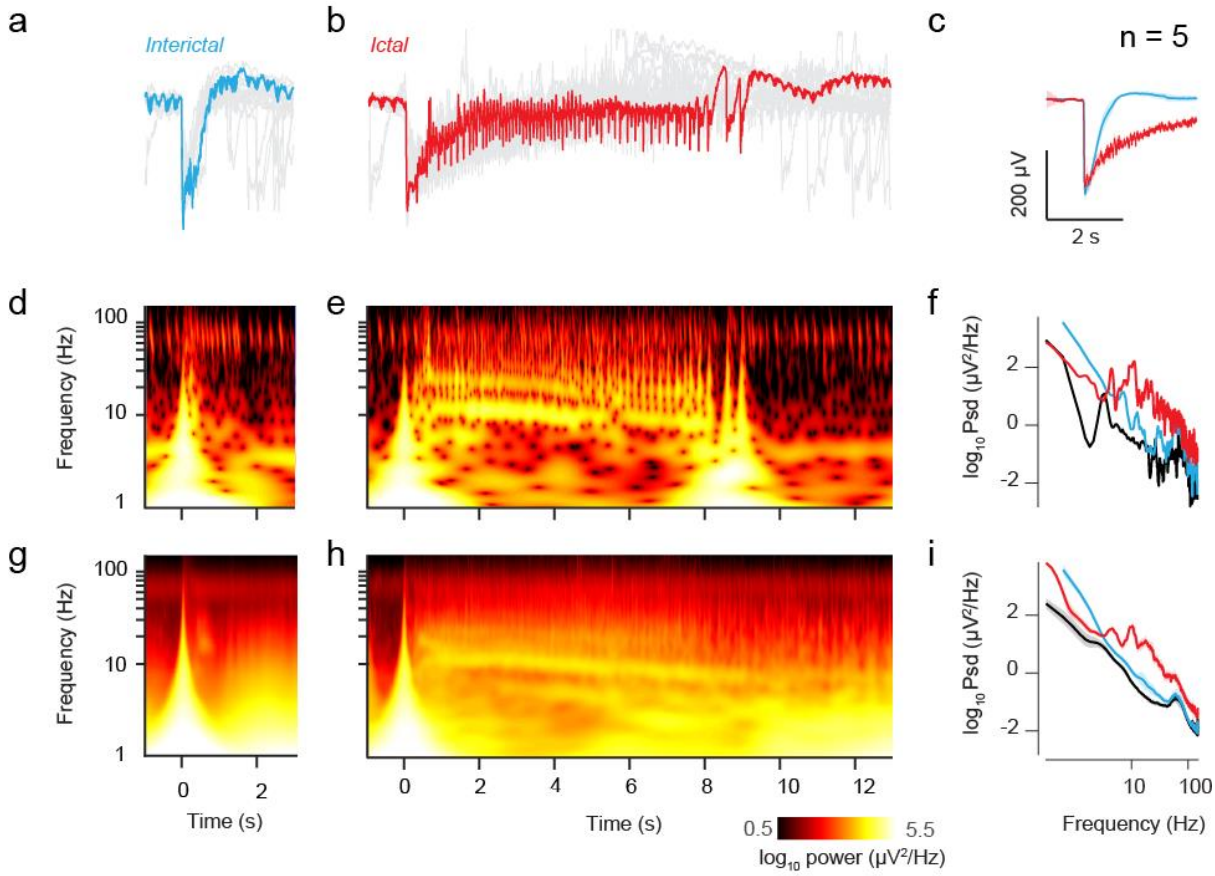

Suppl. Figure 2. Temporal and spectral signatures of interictal events and seizures measured from the LFP. (**a**) LFP waveform of a representative interictal event (blue) and of other example events recorded during the same experiment (gray). (**b**) Same as **a**, for seizures in the same experiment. (**c**) Average across animals (n = 5) of the LFP waveform following the onset of interictal discharges (blue) and seizures (orange). (**d**-**e**) Spectrograms (Morlet-wavelet scalograms) of the representative traces in **a** and **b**. (**f**) Power spectra of those two events measured over 3 s from onset, and compared to a representative baseline period (black). (**g**-**h**) Average spectrogram of interictal events (n = 1476) and seizures (n = 137), across 5 animals. (**i**) Average power spectrum of the events, obtained by averaging curves such as those in **f** across events and animals. The width of the curves indicates 2 s.e.m.

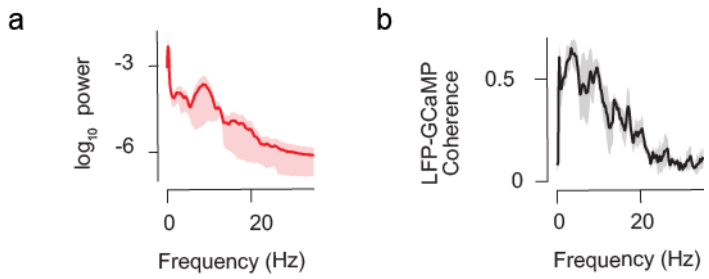

Suppl. Figure 3. Frequency content of GCaMP signals. (**a**) Average power spectrum of the GCaMP signals recorded over the visual cortex during seizures, across animals (n = 4). (**b**) Average coherence between the LFP and the GCaMP signals recorded during seizures across animals (n = 4).

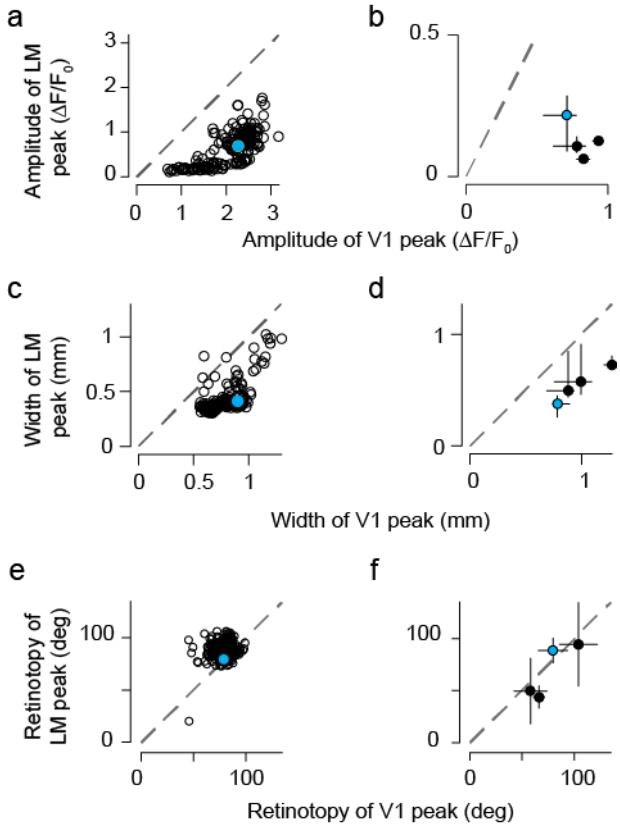

Suppl. Figure 4. Characterizing the two homotopic responses during interictal events. (**a-f**) Response profiles from Figure4 were fit with two Gaussians. The left panels (**a**, **c**, **e**) summarize the fit for each event from the example animal in Figure4; the right panels (**b**,**d**,**f**) show the data from every animal, median ± first quartile. (**a-b**) The peak response in V1 is plotted against the peak response in LM. To allow comparison between different GCaMP variant, data where normalized to the max V1 response in the right panel. (**c-d**) The standard deviation of the Gaussian fit in V1 is plotted against the standard deviation of the fit for LM. (**e-f**) The retinotopic position of the fit in V1 is plotted against the retinotopic position of the peak in LM.

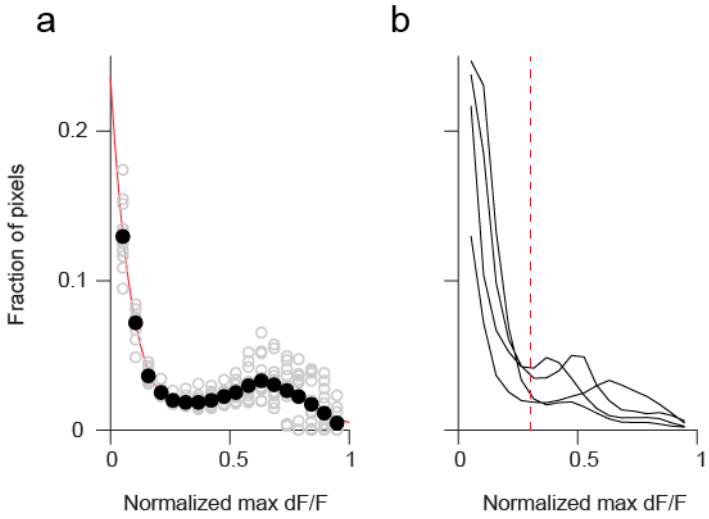

Suppl. Figure 5: Selection of pixels recruited into the seizure. (**a**) Distribution of maximum pixels intensities during seizures for one animal (n= 14), normalized to absolute maximum. Black dot's shows the average distribution, gray dots single trial distribution. Red line is a double Gaussian fit to the average data, individually normalized to absolute maximum. (**b**) Average distribution of maximum pixel intensities during seizures for 4 animals. On average, a threshold of 0.3 (dashed line) separates well the population of pixels with greater activity.

Supplementary movies

Suppl. Movie 1: Example interictal events from 3 example animals. *Leftmost panels*: the retinotopic maps for each example animal. *Right panels*: 4 representative interictal events for each animal. The frame rate is 35 frames/s, two times slower compared to real time. Each event was normalized to its maximum ΔF/F value.

Suppl. Movie 2: Example seizures from 3 example animals. *Left column*: retinotopic maps for each example animal. *Remaining panels*: 4 representative seizures for each animal. The frame rate is 35 frames/s, 2 times slower compared to real time. Each event was normalized to its maximum ΔF/F value.

Suppl. Movie 3: Example cycle average of fast oscillations during one seizure. *Left panel*: cycle average of the filtered 6-11Hz GCaMP oscillation, normalized to maximum and with retinotopic map superimposed. *Right panel*: cycle average of the Hilbert transform phase of the oscillation. The saturation indicates the amplitude of the oscillation for each pixel.